The "RED versus NIR" Plane to Retrieve Broken-Cloud Optical Depth from Ground-Based Measurements

ALEXANDER MARSHAK

Climate and Radiation Branch, NASA Goddard Space Flight Center, Greenbelt, Maryland

YURI KNYAZIKHIN

Department of Geography, Boston University, Boston, Massachusetts

KEITH D. EVANS

Joint Center for Earth System Technology, University of Maryland, Baltimore County, Baltimore, Maryland

WARREN J. WISCOMBE

Climate and Radiation Branch, NASA Goddard Space Flight Center, Greenbelt, Maryland

ABSTRACT

A new method for retrieving cloud optical depth from ground-based measurements of zenith radiance in the red (RED) and near-infrared (NIR) spectral regions is introduced. Because zenith radiance does not have a one-to-one relationship with optical depth, it is absolutely impossible to use a monochromatic retrieval. On the other side, algebraic combinations of spectral radiances, such as normalized difference cloud index (NDCI), while largely removing nonuniqueness and the radiative effects of cloud inhomogeneity, can result in poor retrievals due to its insensitivity to cloud fraction. Instead, both RED and NIR radiances as points on the "RED versus NIR" plane are proposed to be used for retrieval. The proposed retrieval method is applied to Cimel measurements at the Atmospheric Radiation Measurements (ARM) site in Oklahoma. Cimel, a multichannel sun photometer, is a part of the Aerosol Robotic Network (AERONET)—a ground-based network for monitoring aerosol optical properties. The results of retrieval are compared with the ones from microwave radiometer (MWR) and multifilter rotating shadowband radiometer (MFRSR) located next to Cimel at the ARM site. In addition, the performance of the retrieval method is assessed using a fractal model of cloud inhomogeneity and broken cloudiness. The preliminary results look very promising both theoretically and from measurements.

1. Introduction

The most common approach for retrieving cloud optical depth from ground-based observations uses downwelling fluxes measured by pyranometers in the 0.3- to 3.0-μm region of the solar spectrum (Leontieva and Stamnes 1994; Boers 1997). They are relatively cheap and included as standard equipment at many meteorological stations. In addition to broadband pyranometers, there are multifilter rotating shadowband radiometers (MFRSRs) that infer the optical properties of clouds using downwelling fluxes measured at one or at several wavelengths in the visible and/or near-infrared spectral regions (Min and Harrison 1996; Leontieva and Stamnes 1996). The key element in both retrieval techniques is

the one-to-one mapping of the "observed" fluxes into cloud optical depth through (the use of) plane-parallel radiative transfer. Both methods are expected to work well only for completely overcast clouds (Ricchiazzi et al. 1995; Dong et al. 1997), giving an *effective* optical depth for the whole sky since, for inhomogeneous clouds, each sky element contributes to the downwelling flux differently (Boers et al. 2000). To infer cloud optical depth locally, one can assume to use a narrow-field-of-view radiometer that measures radiances instead of fluxes (Pavloski and Ackerman 1999). However, lack of one-to-one relationships between radiance and cloud optical depth (e.g., see Fig. 1 in Barker and Marshak 2001 for zenith radiances) prevents the direct use of radiances also.

Recently, Marshak et al. (2000) and Knyazikhin and Marshak (2000) proposed to exploit the sharp spectral contrast in vegetated surface reflectance across 0.7-μm wavelength to retrieve cloud properties from ground-

Corresponding author address: Alexander Marshak, Code 913, NASA GSFC, Greenbelt, MD 20771.
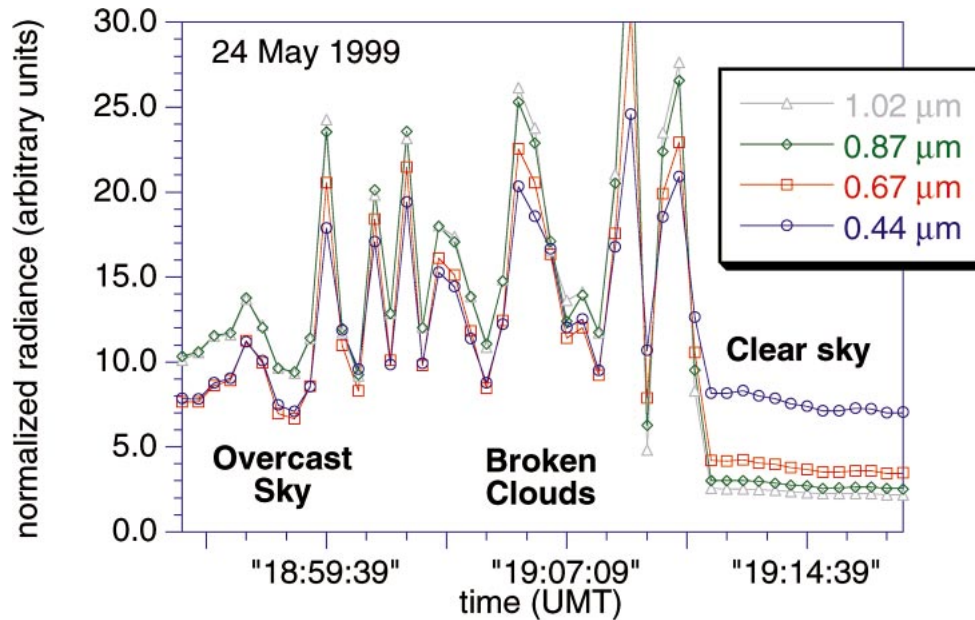E-mail: Alexander.Marshak@nasa.gov

FIG. 1. Zenith radiance measured by a Cimel sun photometer at Greenbelt, MD, on 24 May 1999. Four channels (0.44, 0.67, 0.87, and 1.02 μm) are used. The measured radiance is normalized by the solar flux at the top of atmosphere (TOA) in the corresponding spectral interval.

based radiance measurements. The idea is to use ground zenith radiance measurements in two narrow spectral bands on each side of the sharp jump in vegetation albedo near 0.7 μm. Below 0.7 μm in the red (RED) spectral region (648–680 nm), the chlorophyll in green leaf absorbs 90%–95% of solar radiation; thus, the vegetation albedo is low. On contrast, above 0.7 μm in the near-infrared (NIR) spectral region, a green leaf reflects about 90% of incident radiation resulting in a high value of the albedo of vegetated surfaces. In the NIR region, therefore, the green vegetation acts as a powerful reflector illuminating horizontally inhomogeneous clouds from below (see Fig. 5 in Marshak et al. 2000). This provides the extra information needed to largely remove the ambiguity in measured downwelling radiance caused by radiative effects of the three-dimensional (3D) cloud structure.

The spectral index proposed by Marshak et al. (2000) while substantially eliminating the effect of 3D cloud structure does not carry information on cloud fraction and, in general, cannot correctly account for the total amount of radiation reaching the surface. Thus, in addition to zenith radiances, Barker and Marshak (2001) suggested to use downwelling spectral fluxes measured at the surface or from aircraft-based radiometers (Barker et al. 2002). Knowledge of downwelling fluxes substantially improves the retrieval though limits its applicability to sites equipped with MFRSR or other spectral flux measured radiometers.

Here we propose a new method for inferring cloud optical depth from spectral zenith measurements without requiring simultaneous measurements of spectral fluxes.

Thus, it can be used to monitor clouds from remotely located Cimel multichannel sun photometers that are the main part of the Aerosol Robotic Network (AERO-NET)—a ground-based monitoring network that consists of identical multichannel radiometers for assessing aerosol optical properties and validating their satellite retrievals (Holben et al. 1998).

The idea of the method comes from the "RED versus NIR" method used to retrieve leaf area index (LAI) from satellite measurements (Knyazikhin et al. 1998; Shabanov et al. 2002). In addition to cloud optical depth, the new retrieval method also infers a "radiatively effective" cloud fraction. A similar approach in satellite remote sensing is the Nakajima–King technique for retrieving cloud optical depth and effective particle radius from satellite data (Nakajima and King 1990).

The plan of the paper is as follows. We start from the physical background deduced from Cimel measurements under clear and cloudy conditions (section 2); then we discuss cloud index and its shortcomings (section 3). In section 4 a new retrieval technique is introduced that then is applied to Cimel data (section 5). Surface reflective properties as key parameters in the retrieval technique are discussed in section 6, while in section 7 the method is validated using a fractal-based model of cloud inhomogeneity. Finally, in section 8 the results are summarized.

2. Three main atmospheric cases observed in ground zenith radiance measurements

For proof-of-concept measurements (Wiscombe et al. 2000), Fig. 1 shows a 22-min fragment of zenith radi-

ance measured by a ground-based Cimel multichannel sun photometer pointed straight up. Cimel has a narrow field of view of 1.2° and four filters at 0.44, 0.67, 0.87, and 1.02 μm that are designed for retrieving aerosol properties in clear-sky conditions. In our example, Cimel measured radiance at 20-s temporal resolution.

There are three distinct regions in Fig. 1: (from left to right) a single unbroken cloud, broken clouds, and a clear sky. For clear-sky conditions, due to Rayleigh scattering and optically thicker aerosol at shorter wavelengths, zenith radiance increases with a decrease in the wavelength from 1.02 to 0.44 μm. By contrast, for cloudy conditions, radiances in channel 0.44 and 0.67 μm are almost indistinguishable; this is also true for channels 0.87 and 1.02 μm. This is a clear indication that, in the presence of clouds, the spectral contrast in surface albedo dominates over Rayleigh and aerosol effects. In contrast to the small fluctuations typical for clear and even cloudy skies, broken clouds show sharp changes in radiances around cloud edges.

To be more formal, based on photon cloud–vegetation interactions we distinguish three main cases.

1) *Atmosphere dominates.* In this case,

$$I_{0.44} \gg I_{0.67} > I_{0.87} > I_{1.02}, \qquad (1a)$$

and aerosol optical properties can be retrieved.
2) *(Vegetated) surface and cloud dominate.* In this case,

$$I_{0.44} \approx I_{0.67} < I_{0.87} \approx I_{1.02}, \qquad (1b)$$

and cloud optical properties can be retrieved given the surface albedo.
3) *Transition between the first two cases* is characterized by rapid changes between the "order" of I_λ from cloudy to clear and back. In this case, neither aerosol nor cloud properties can be reliably retrieved using only *one* wavelength. However, as will be seen below, the two-wavelength retrieval for broken clouds can be almost as successful as for an overcast sky.

3. Cloud index and its shortcoming

By analogy with the normalized difference vegetation index (NDVI; Tucker 1979; Verstraete and Pinty 1996), Marshak et al. (2000) and Knyazikhin and Marshak (2000) proposed to use the normalized difference cloud index (NDCI) defined as a ratio between the difference and the sum of two normalized zenith radiances measured for two narrow spectral bands in the NIR (0.87 μm) and RED (0.67 μm) spectral regions:

$$\text{NDCI} = \frac{I_{\text{NIR}} - I_{\text{RED}}}{I_{\text{NIR}} + I_{\text{RED}}}. \qquad (2)$$

Compared to a two-valued optical depth versus zenith radiance relationship that makes its retrieval absolutely impossible [see one-dimensional (1D) curves in Figs. 2a and 2b], the NDCI is a monotonic function with

respect to optical depth (see a 1D curve in Fig. 2c). In contrast to any conventional method of estimating cloud optical depth from the surface that uses either broadband (Leontieva and Stamnes 1994) or a single wavelength (Min and Harrison 1996) and is expected to work well only for overcast clouds (Boers et al. 2000), the NDCI-based retrieval technique is much less sensitive to cloud structure. The sensitivity is weak because the NDCI-based method eliminates the part of downward radiation that did not have interactions with surface; this radiation is the most sensitive to both illumination conditions and cloud inhomogeneity (Marshak et al. 2000; Barker and Marshak 2001). In addition, the NDCI is almost insensitive to the solar zenith angle (SZA); consequently, optical depth of a cloud illuminated under SZA = 80° can be retrieved as accurately as the one illuminated under SZA = 45°. This is a valuable feature of a retrieval method since most current techniques fail to perform reliable retrievals for large SZA. The NDCI-based approach first extracts radiation reflected by clouds and then performs retrieval, hence its weak sensitivity to the SZA (cf. to Kaufmann et al. 2000 for NDVI).

As follows from Eqs. (1a)–(1b), the NDCI will be negative for a clear sky and positive for an overcast sky. In case of broken clouds, NDCI can take on either positive or negative values, depending whether or not there is a cloud in the zenith direction.

The first shortcoming of the NDCI-based retrieval technique comes from the underestimation of zenith radiance for large optical depth in NIR. Indeed, Figs. 2a and 2b show 3D and 1D zenith radiances calculated for black (RED) and bright (NIR) surface. We see that in the RED spectral region, 3D radiances are scattered around a theoretical 1D curve, while in NIR, 1D radiance systematically underestimates 3D radiances for large optical depths. This has a simple interpretation: for 3D clouds, more radiation is transmitted through; thus, more radiation is reflected back from thick clouds to the surface.

Another shortcoming innate to all spectral-indices-based concepts is that the spectral information is reduced to one number by an algebraic transformation (e.g., Diner et al. 1999; Tian et al. 2000). In other words, instead of *two* spectral values of zenith radiances in RED and NIR, only *one*, NDCI, is used. Indeed, each measurement can be depicted as a point on the RED versus NIR plane, which has two coordinates:

$$\eta = \sqrt{I_{\text{RED}}^2 + I_{\text{NIR}}^2}, \qquad (3a)$$

$$\alpha = \arctan(I_{\text{RED}}/I_{\text{NIR}}). \qquad (3b)$$

Both coordinates can depend on the cloud optical depth. However, the NDCI,

$$\text{NDCI} = \frac{1 - \tan\alpha}{1 + \tan\alpha}, \qquad (3c)$$

is a function of α only, and thus cloud optical depth can vary considerably with NDCI unchanged. We will
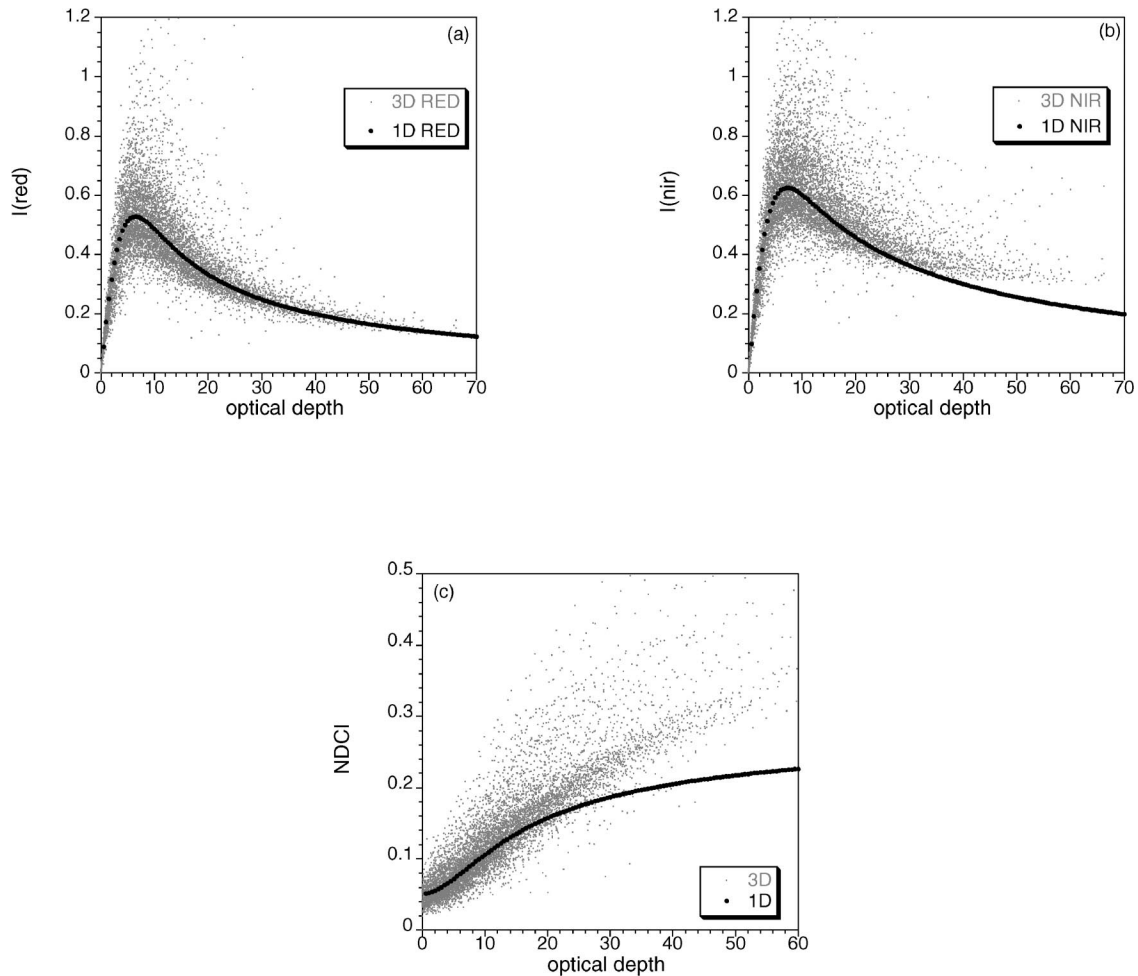
FIG. 2. Downward radiances calculated by Monte Carlo methods for (a) "black" surface (RED, $\rho = 0.0$), and (b) "bright" surface (NIR, $\rho = 0.5$). Pixel size is 25 m, SZA = 60°, $\varpi_0 = 1.0$. Henyey–Greenstein scattering phase function is used. Horizontal distribution of cloud optical depth is simulated by a 10-step bounded cascade model (Cahalan 1994; Marshak et al. 1994) with parameters $\langle \tau \rangle = 13$, $\beta = 1.4$, and $p = 0.35$. The average geometrical cloud thickness is 300 m; cloud-base height is 1 km. Gaps are added as in Marshak et al. (1998). The results of 1D radiative transfer calculations from DISORT (Stamnes et al. 1988) are added for convenience. (c) The same as (a) and (b), but for the NDCI defined by Eq. (2).

show below how this shortcoming can be overcome if both NIR and RED wavelength are used instead of the NDCI.

4. RED versus NIR plane

Any ground measurements of radiance I can be represented as a sum of two components (e.g., Box et al. 1988): the radiation calculated for a nonreflecting surface I_0 and the radiation due to surface–cloud interactions:

$$I = I_0 + \frac{\rho T_0 I_s}{1 - \rho R}. \tag{4}$$

Here, R is the spherical albedo for isotropically illuminated from below clouds, T_0 is the transmittance for nonreflecting surface, and I_s is the radiance of a radiation field generated by an isotropic source $1/\pi$ located at the surface, and ρ is albedo of the underlying Lambertian surface.

Following Barker and Marshak (2001), we will define T_0 as

$$T_0 = T_{\text{clear}}(1 - A_c) + T_{\text{cloudy}}A_c, \tag{5}$$

where A_c is a cloud fraction. Assuming for simplicity that $T_{\text{clear}} = 1$, $T_{\text{cloudy}} = T_{0\text{pp}}$, where $T_{0\text{pp}}$ is plane-parallel transmittance for nonreflecting surface. Then Eq. (5) can be rewritten as

$$T_0 = 1 - A_c + T_{0\text{pp}}A_c. \tag{6}$$

In contrast to a vegetation canopy, variation in cloud optical properties between 0.66 and 0.87 μm are small and, as a first approximation, they can be assumed to be wavelength independent. Thus the variables I_0, I_s, T_0, and R will be functions of cloud optical depth τ
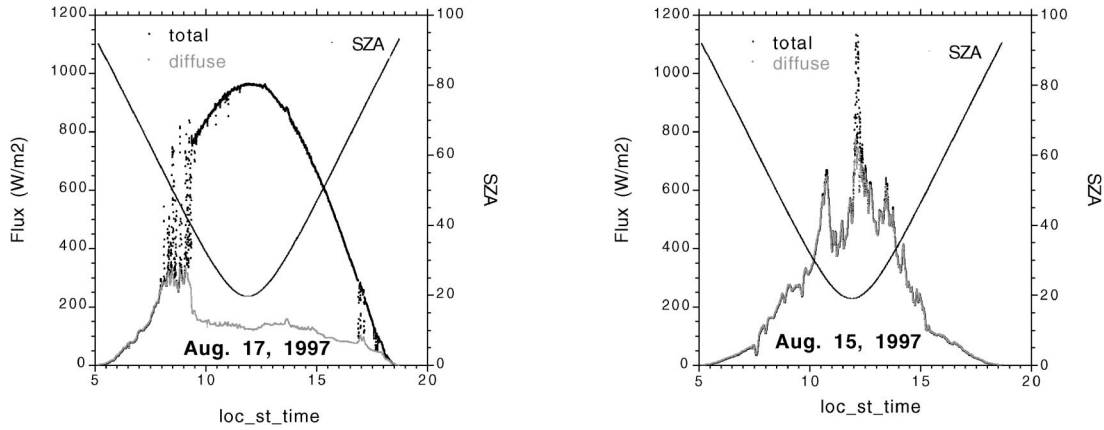
FIG. 3. Ground-based measurements of broadband downward radiation at La Jolla, CA, for 2 days in Aug 1997 (courtesy of E. Dutton). (left) Typical for La Jolla: early morning overcast sky, then broken cloudiness that clears up by noon. (right) An almost entirely overcast day with a few scattered clouds around noon. Solar zenith angles are added for clarity.

only. The surface albedo ρ is the only variable that imbues wavelength dependence to Eq. (4). It follows from these assumptions and from (6) that

$$I_{\mathrm{RED}}(\tau, A_c) = I_0(\tau) + \frac{\rho_{\mathrm{RED}}I_s(\tau)[1 - A_c + A_c T_{0\mathrm{pp}}(\tau)]}{1 - \rho_{\mathrm{RED}}R(\tau)}$$

(7a)

and

$$I_{\mathrm{NIR}}(\tau, A_c) = I_0(\tau) + \frac{\rho_{\mathrm{NIR}}I_s(\tau)[1 - A_c + A_c T_{0\mathrm{pp}}(\tau)]}{1 - \rho_{\mathrm{NIR}}R(\tau)}.$$

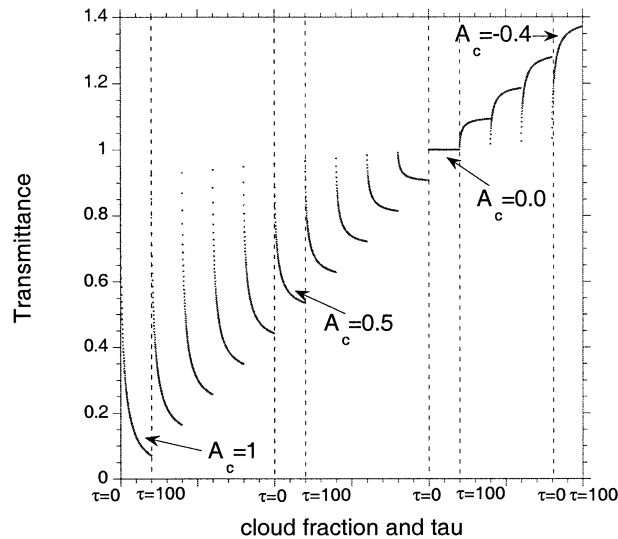(7b)

Let us consider Eq. (6). It is easy to show that

FIG. 4. Transmittance T_0 as a function of optical depth τ and cloud fraction A_c. Horizontal axis consists of 15 ranges of τ from 0 to 100. Each τ range corresponds to different A_c from $A_c = 1$ to $A_c = -0.4$, including the case of $A_c = 0$, which corresponds to $T_0 \equiv 1$.

$$0 \leq T_{0\mathrm{pp}} \leq T_0 \leq 1 \qquad (8)$$

if

$$0 \leq A_c \leq 1. \qquad (9)$$

The middle inequality in (8) expresses a common knowledge that transmittance for inhomogeneous (or broken) clouds is larger than its plane-parallel counterpart. However, it is also known that for broken clouds transmittance can exceed unity because of photons scattered downward from cloud edges. Thus the last inequality in (8) is not necessarily hold for broken clouds. Figure 3 illustrates this. We can clearly see that downward flux for broken clouds [between 0800 and 1000 local time (LT) 17 August and around 1200 LT 15 August] exceeds the one for clear sky, thus producing transmittance larger than 1. More precisely, at 1203 LT and SZA = 19.4 on 15 August, the transmittance exceeds 1.15. Can this effect be simulated in the frame of plane-parallel radiative transfer?

Let A_c account not only for a fraction of cloudy pixels in the whole sky but also for photon horizontal transport (e.g., Titov 1998; Marshak et al. 1999) ignored by 1D radiative transfer. Therefore, A_c will be not a "real" cloud fraction but rather a "radiatively effective" one that forces plane-parallel radiative transfer calculations to give the same values of I_{NIR} and I_{RED} as the measured (3D) ones. In this case, one may release condition (9) and allow A_c to be *negative*. Then it immediately follows from Eq. (6) that T_0 may exceed 1 and will be able to simulate reflectance from cloud edges. Not surprisingly that in this case, T_0 as a function of optical depth looks more like reflectance than transmittance (convex versus concave). Figure 4 shows T_0 as a function of τ and A_c. Note that $A_c = 0$ gives $T_0 \equiv 1$, while negative A_c correspond to $T_0 > 1$.

To illustrate this behavior, Fig. 5a shows an 8-km fragment of a simulated broken cloud field. As expected, the cloud edge around 38.4 km looks much brighter
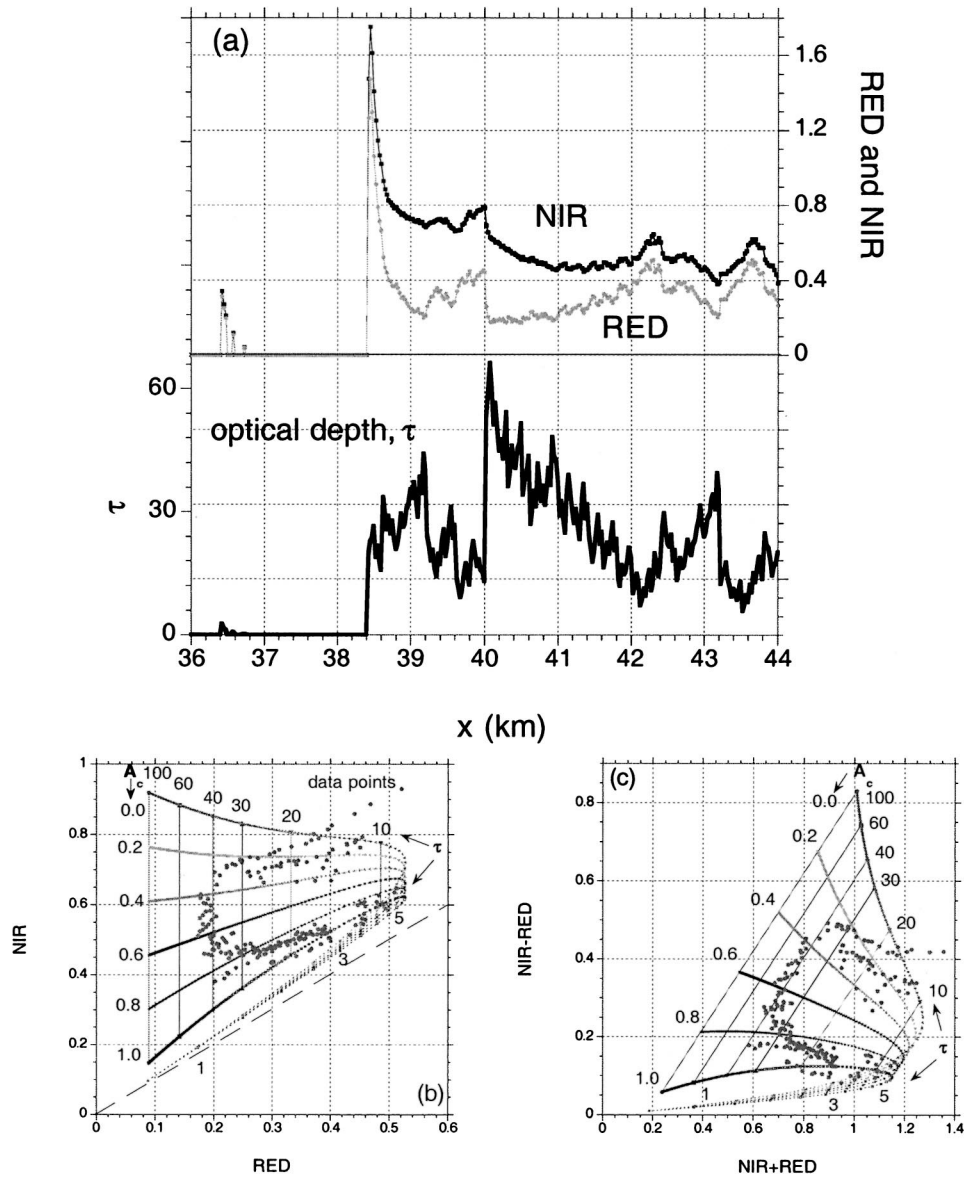
FIG. 5. Zenith radiances I_{RED} and I_{NIR} for the same model as in Fig. 2. (a) An 8-km fragment of I_{RED}, I_{NIR} (top, right vertical axis) and optical depth τ (bottom, left vertical axis) vs horizontal position x (km). (b) Zenith radiances for RED and NIR as functions of τ and A_c [Eqs. (7a) and (7b)] calculated using DISORT; τ changes from 0.5 to 100, while A_c changes from 0.0 to 1.0. Note that both I_{RED} and I_{NIR} are double-valued functions with respect to τ. Dots corresponds to data points from (a) between 38.6 ($I_{NIR} < 1.0$) and 43.6 km (200 dots). (c) The same as in (b), but for $I_{NIR} - I_{RED}$ vs $I_{NIR} + I_{RED}$.

than the rest of the cloud for both RED and NIR radiation. However, when one moves away from the cloud edge, I_{RED} decays much faster than I_{NIR}. Only about 300 m away from the edge, I_{RED} has been already stabilized while I_{NIR} is still strongly affected by the illumination by the bright surface. [Note from the 1D curves in Figs. 2a and 2b that $\max(I_{RED}) = 0.53$, while $\max(I_{NIR}) = 0.62$.] No positive A_c is able to model this effect in the frame of plane-parallel theory. Indeed, Fig. 5b shows a 2D lookup table (LUT) of I_{NIR} versus I_{RED} as functions of τ and A_c described by Eqs. (7a)–(7b). We see that a

few data points that are above the $A_c = 0$ curve need negative A_c to be matched by 1D calculations. Obviously, these data points correspond to transmittance $T_0 > 1$. Also note that all cloudy data points as well as the LUT itself is above the diagonal $I_{NIR} = I_{RED}$; that is, $I_{NIR} > I_{RED}$. The same data points and LUT will occupy the whole plane if the difference $I_{NIR} - I_{RED}$ is plotted against I_{RED} or the sum $I_{NIR} + I_{RED}$. The latter one (Fig. 5c) is preferable since any line through the origin point (0,0) corresponds to NDCI defined in Eq. (2).
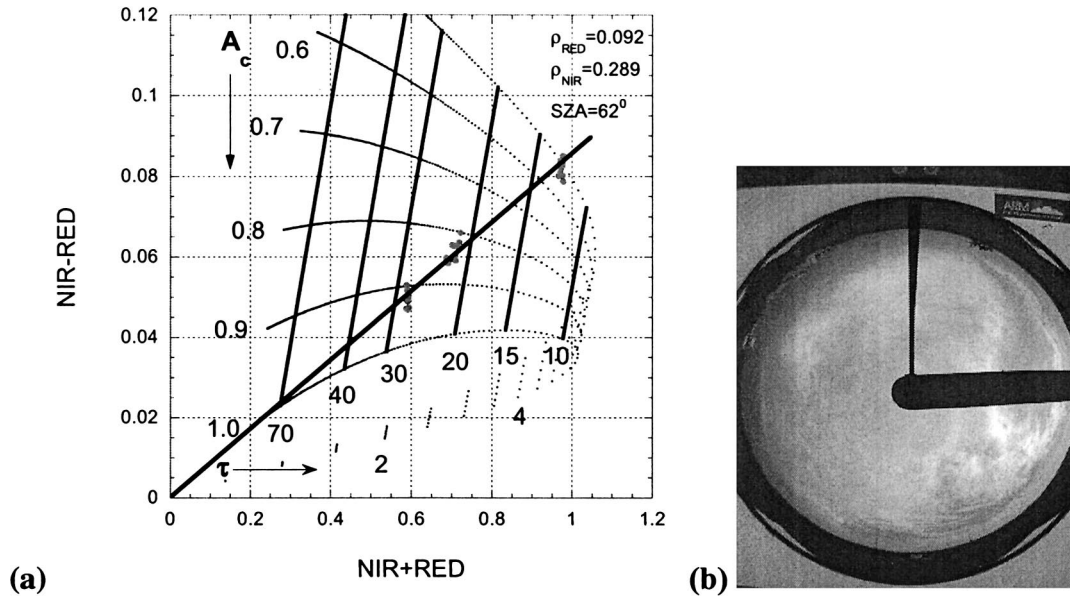
FIG. 6. (a) DISORT-calculated values of $I_{NIR} + I_{RED}$ and $I_{NIR} - I_{RED}$ for a wide range of τ and A_c for SZA = 62° ± 3° and surface albedos $\rho_{RED} = 0.092$ and $\rho_{NIR} = 0.289$. When A_c is constant and τ is varying, the set of calculated values define the cloud fraction isoline or trajectory. When τ is constant and cloud fraction is varying, the set of values define the τ isolines. Values $I_{NIR} + I_{RED}$ and $I_{NIR} - I_{RED}$ (30 dots with 10 for each cluster) are from Cimel measurements at the ARM site in Oklahoma on 28 Jul 2002. Measurements were taken around 1345, 1358, and 1411 UTC, respectively (toward decreasing NIR + RED). A straight line through (0,0) corresponds to the NDCI ≈ 0.08. (b) Total sky image taken at 1400 UTC with SZA = 62.75°.

As an example, Fig. 6a shows a NIR − RED versus NIR + RED plane with Cimel measurements at the Atmospheric Radiation Measurements (ARM) site in Oklahoma (36.61°N, 97.48°W) on 28 July 2002. For SZA = 62° and surface albedos $\rho_{RED} = 0.092$ and $\rho_{NIR} = 0.289$, it illustrates a discrete ordinates radiative transfer (DISORT) calculated LUT with I_{NIR} and I_{RED} as functions of τ and A_c, and three groups of data points (10 points per group; see next section for explanations) measured by Cimel. The data points, while having different values of I_{NIR} and I_{RED}, thus being located at different positions on the plane, have almost the same NDCI [a straight line through the point (0, 0)] and hence, if retrieved from it, would have the same optical depth τ (80 for $A_c = 1.0$). However, as follows from the LUT, these groups correspond to different pairs—($A_c = 0.9$; $\tau = 28$), ($A_c = 0.8$; $\tau = 22$), and ($A_c = 0.4$; $\tau = 12$)— and thus have different optical depths. Figure 6b shows a total sky image (TSI) picture taken at 1400 UTC close to the middle cluster of points in Fig. 6a. Note that $A_c = 0.8$ is not a real cloud fraction but a radiatively effective one that also compensates for cloud horizontal inhomogeneity not accounted by 1D radiative transfer.

The LUTs shown in Fig. 6 and Figs. 5b and 5c for retrieval cloud optical depth and cloud fraction can be viewed as a ground-based counterpart of the Nakajima–King retrieval of cloud optical depth and effective particle radius from reflected solar radiation (Nakajima and King 1990). In the Nakajima–King retrieval, the visible channel is more sensitive to cloud optical depth and less

sensitive to particle size while the absorbing NIR channel is more sensitive to particle size than to optical depth. Similarly, for the ground-based retrieval above vegetation, the RED channel is much more sensitive to optical depth while the NIR is more sensitive to cloud fraction. The next section will discuss the retrievals in more detail.

5. Retrieval from Cimel measurements

The Cimel spectrometer is the main instrument in the AERONET—a ground-based monitoring network that consists of identical multichannel radiometers for assessing aerosol optical properties and validating satellite retrievals (Holben et al. 1998). Based on the above ideas, we have developed a method for Cimels to monitor cloud optical depth by using "idle time" inappropriate for aerosol studies for taking measurements of zenith radiance at 0.44, 0.67, 0.87, and 1.02 μm. Every 15 min, if the sun is blocked by clouds, the Cimel points straight up and takes 10 measurements with a 9-s time interval.

The main idea of our method is to retrieve cloud optical depth using both 0.67-μm (RED) and 0.87-μm (NIR) zenith radiances; surface albedos ρ_{RED} and ρ_{NIR} are assumed to be known from independent measurements. The other two channels (0.44 and 1.02 μm) are used to select cases where the spectral contrast in surface albedo dominates over Rayleigh and aerosol effects [i.e., when Eq. (1b) is held] and the proposed method will
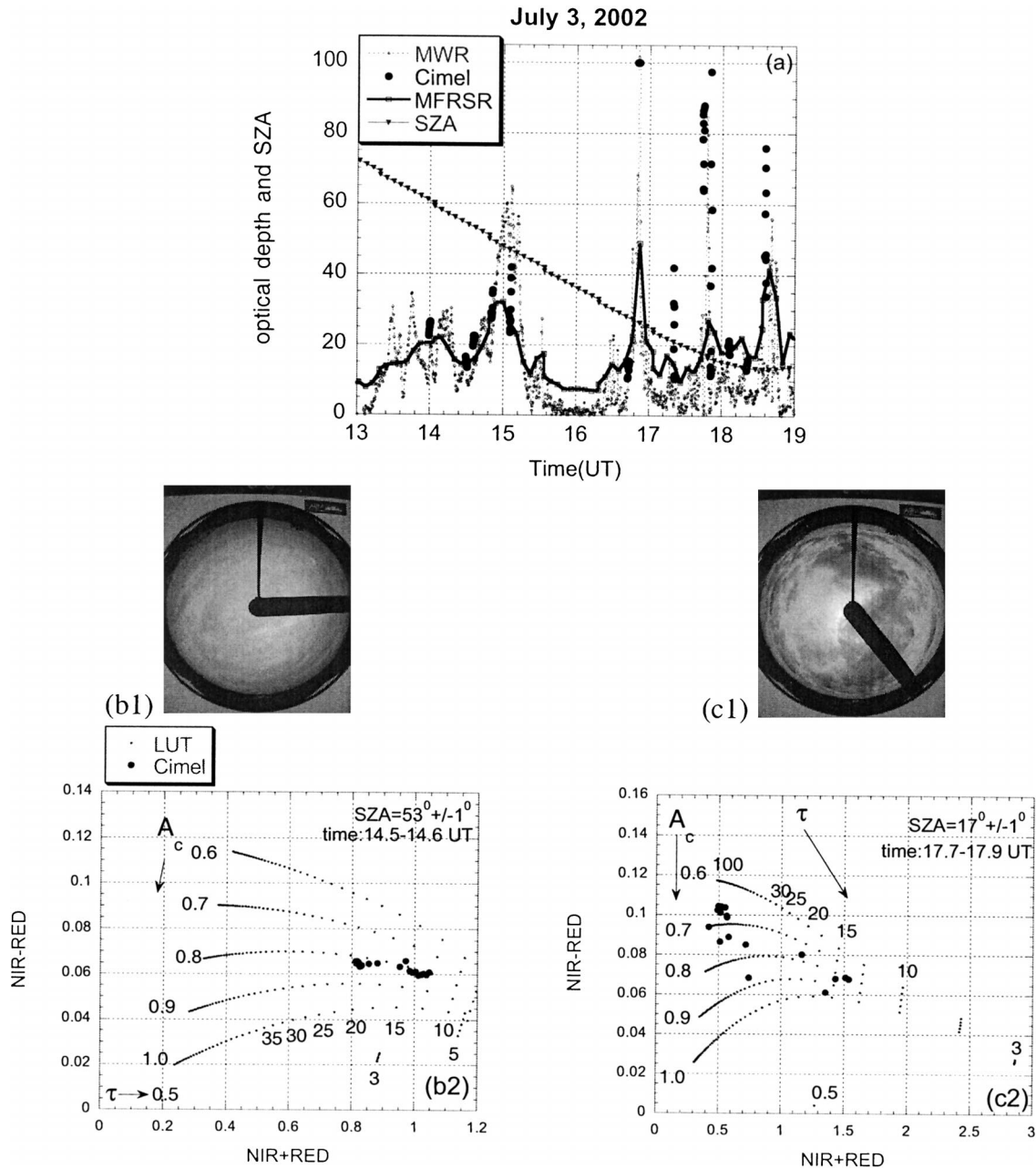
FIG. 7. Retrievals for 3 Jul 2002 at the ARM Oklahoma site: (a) cloud optical depth retrieved from MWR (assuming droplet effective radius of 7 μm), MFRSR fluxes [using algorithm proposed in Min and Harrison (1996)], and Cimel radiances (using reflectances from a vegetated surface with albedos ρ_{RED} = 0.119 and ρ_{NIR} = 0.302). SZA is added for convenience. (b1) Total sky image for SZA = 52.3° taken at 1436 UTC. (b2) LUT for SZA = 53° ± 1°. Optical depth τ changes from 0.5 to 100 with increments of 2.5, while cloud fraction A_c changes from 0.6 to 1.0 with increment of 0.1. Twenty dots correspond to Cimel measurements taken between 1430 and 1437 UTC. (c1) The same as in (b1), but for SZA = 16.3° taken at 1750 UTC. (c2) The same as in (b2), but for SZA = 17° ± 1°. Twenty Cimel measurements were taken between 1743 and 1752 UTC.

likely work. Another consistency check is related to Cimel's second collimator that has the same field of view of 1.2° but 10 times larger aperture; thus it sees different cloud pieces.

Figure 7a illustrates the retrieval of cloud optical depth from Cimel measurements using the above meth-od. The retrieved optical depths are also compared with the ones from microwave radiometer (MWR; assuming a constant droplet effective radius of 7 μm, which is more typical for the ARM site than a "generic" 10 μm) and from MFRSR [courtesy of Q. Min; for details see Min and Harrison (1996)]. Note that values plotted for

τ from MWR are at 20-s resolution, while those from MFRSR are 5-min averages. For this overcast day, generally we see very good agreement, though there are a few discrepancies. For the most homogeneous plane-parallel cloud around 1430 UTC (Fig. 7b1) all three methods show similar optical depth τ around 15; the LUT in Fig. 7b2 estimates the radiatively effective cloud fraction A_c as 0.85. For more inhomogeneous though still overcast clouds as the one at 1750 UTC (Fig. 7c1), the agreement is not as good as for the homogeneous cloud since MFRSR retrieves a more effective optical depth (in its field of view) than our algorithm does. Figure 7c2 shows the LUT with scattered Cimel dots; the most inhomogeneous part (at 1744 UTC) corresponds to the largest difference between I_{NIR} and I_{RED} that estimates $A_c \approx 0.65$ and $\tau \approx 80$.

Another example (Fig. 8a) corresponds to broken clouds (Figs. 8b and 8c). There are two remarkable features in this day. First, the optical depth is retrieved for SZA $= 81°$ (at 1230–1240 UTC; see Fig. 8b). Most of satellite and ground-based retrieval techniques fail to produce optical depth under such an illumination condition. Second, successful retrievals have been performed for very broken-cloud conditions: the cloud optical depth for 30 min jumps from almost 0 (1752 UTC) to 90 (1808 UTC) and then back to clear sky (1822 UTC). This is also shown in Fig. 8d, where we see the rapidly changing order of Cimel zenith radiances as in Fig. 1 and Eqs. (1a)–(1b). As expected, the optical depth field retrieved from MFRSR around 1800 UTC is much smoother and represents an "effective" optical depth for the sky shown in Fig. 8c.

6. Surface

Since the retrieval algorithm is based on surface–cloud interaction, knowledge of surface reflectance and its heterogeneity around Cimel is absolutely crucial for the success of the algorithm.

The surface albedo was obtained from the Moderate Resolution Imaging Spectroradiometer (MODIS) 16-day Albedo (MOD43B) product (Schaaf et al. 2002) and Multiangle Imaging Spectroradiometer (MISR) surface parameters product (Bothwell et al. 2002). Figure 9 illustrates the MODIS albedo for 0.648 and 0.858 μm around the ARM site for 28 July 2002. The average values are about 0.09 for 0.648 μm and 0.29 for 0.858 μm; they are consistent with the MISR albedo retrieved on 24 July 2002 [$\rho_{0.672} = 0.12$, $\rho_{0.867} = 0.28$; averaged over (27.5 km)^2: $\langle\rho_{0.672}\rangle = 0.10$ with standard deviation (std dev) $= 0.02$ and $\langle\rho_{0.867}\rangle = 0.28$ with std dev $= 0.03$]. Pavloski et al. (2002) used MISR surface albedo data to retrieve cloud optical depth from simultaneous measurements of downward radiance and flux at the ARM site in Oklahoma applying the algorithm proposed by Barker and Marshak (2001).

For the theoretical study based on cloud fields inferred from Landsat imagery, Barker and Marshak (2001) found that as long as the uncertainties in surface albedo have the same sign (both are either overestimated or underestimated), the algorithm performs well. Furthermore, when the NIR albedo is overestimated but the RED albedo is underestimated, errors in the retrieved optical depth are not severe. However, in the opposite case, the algorithm underestimates multiple reflectance in the bright band and greatly overestimates optical depths. Similar tendencies are also valid for the present algorithm. Figure 10 illustrates them for the conditions of 3 July 2002 (see Fig. 7a). We see that errors in optical depth near the diagonal are small and the method performs well. Its performance substantially deteriorates when the RED albedo is overestimated and the NIR albedo is underestimated (the right bottom corner). The uncertainties in both spectral albedos of 0.025 (this is about 8% of NIR and 25% of RED albedos) with the same sign resulted on average 2%–3% errors in the retrieved τ, while with the opposite sign, the retrieved τ on average were underestimated by 4% or overestimated by 9%, depending of whether we increased or decreased the spectral contrast in surface albedo.

Surface reflectance at the ARM site in Oklahoma is very heterogeneous (Li et al. 2002). Figure 11 is based on solar spectral flux radiometer (SSFR) data (Pilewskie et al. 1998) reported in Michalsky et al. (2003). It shows surface albedo in RED and NIR spectral regions measured on flight legs covering the area of about 25 km around the ARM site (Fig. 11a) on 5 April 2000. In addition, data for the nearest 0.0001 rad (about 600 m) to the site was also selected. We see that the range of surface albedos in the area of 1 km around Cimel on that day was from 0.056 to 0.118 for the RED and from 0.325 to 0.434 for the NIR with $\rho_{RED} = 0.085 \pm 0.013$ and $\rho_{NIR} = 0.375 \pm 0.021$. These average results do not necessarily match surface albedo measured from 10- and 25-m towers located exactly at the ARM site over wheat and (dead) grass (Li et al. 2002; Michalsky et al. 2003). However, the big range in surface albedos does not prevent the use of the proposed method since the contribution from surface is integrated over several kilometers (depending on cloud-base height) and the local surface properties are less important than its average or effective characteristics (Knyazikhin and Marshak 2000). It can be shown that in spite of strong surface heterogeneity the value of surface reflectivity around the ARM site stabilizes after averaging over 1–2 km for both RED and NIR spectral regions (Wiscombe et al. 2000).

When the contrast between RED and NIR albedo is small, the uncertainties in surface albedo may lead to unacceptably large errors in the retrieved cloud optical depth. To decide whether or not the above retrieval method is applicable, one needs to set an applicability threshold. As a threshold, the NDVI values available from MODIS can be chosen; for example, for surfaces with NDVI < 0.4 the retrieved values of cloud optical depth are not reliable and retrievals are not performed. For example, for the AERONET site in Bondville, Il-
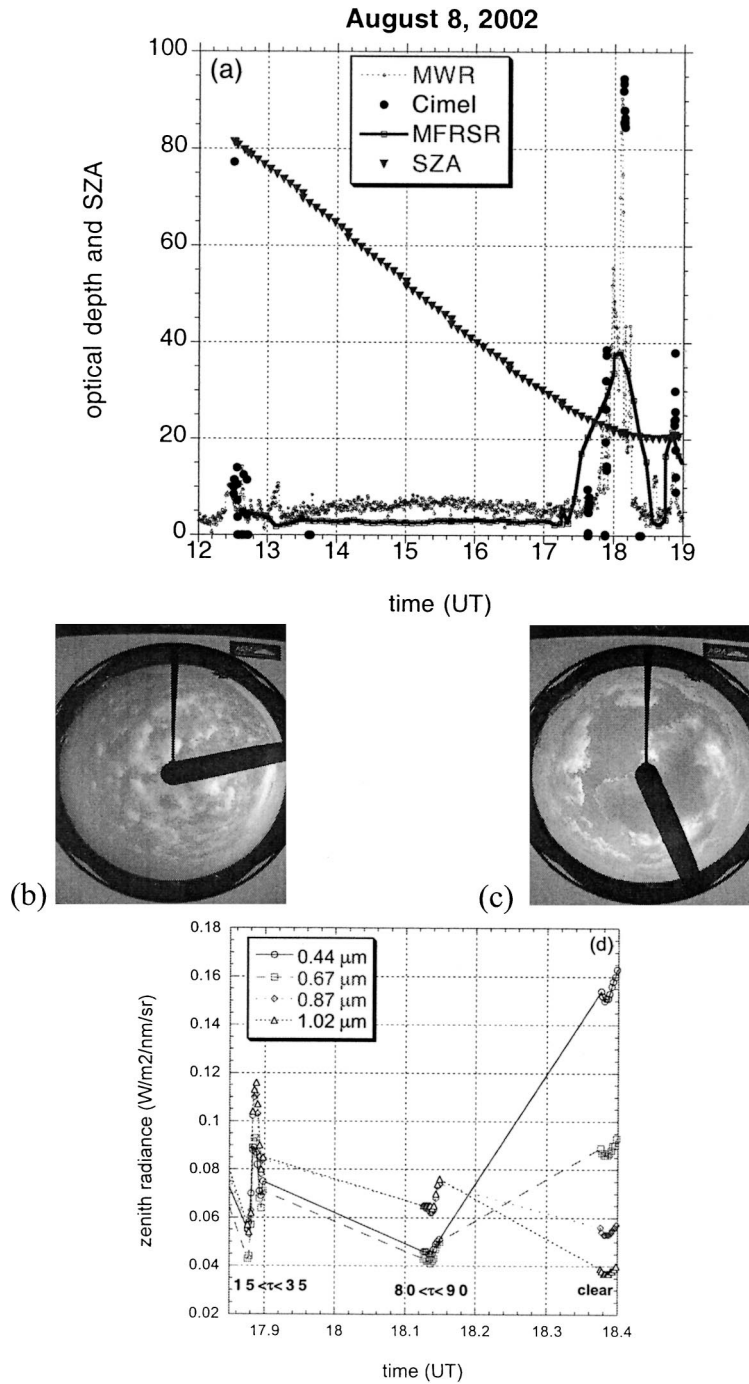
FIG. 8. Retrievals for 8 Aug 2002 at the ARM Oklahoma site: (a) cloud optical depth retrieved from MWR (assuming droplet effective radius of 7 μm), MFRSR [Min and Harrison (1996)] averaged over 5 min, and Cimel radiances (surface albedos are $\rho_{RED} = 0.096$ and $\rho_{NIR} = 0.338$). Solar zenith angle is added for convenience. (b) Total sky image for SZA = 79.6° taken at 1240 UTC. (c) The same as in (b), but for SZA = 21.9° taken at 1800 UTC. (d) Thirty minutes of normalized Cimel zenith radiances at four channels: 0.44, 0.67, 0.87, and 1.02 μm.
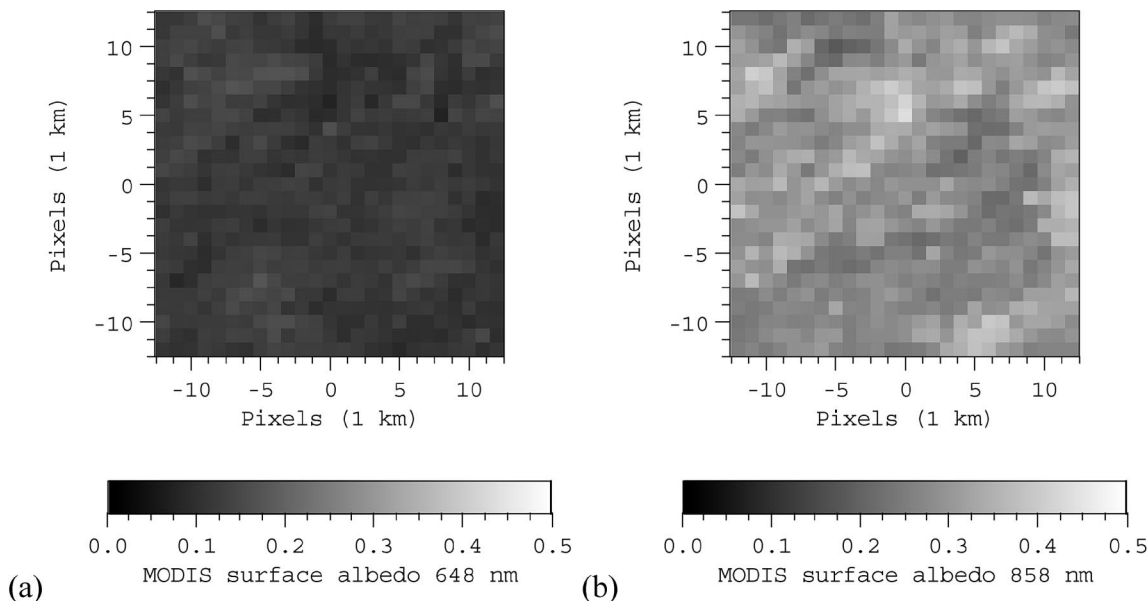
FIG. 9. Surface albedo retrieved from MODIS on 28 Jul 2002: 25 km × 25 km area around the ARM site in Oklahoma [location is at (0,0)]; (a) 0.648 μm, at the ARM site $\rho_{0.648} = 0.092$, averaged over (25 km)^2 $\langle \rho_{0.648} \rangle = 0.091$ with std dev = 0.016; (b) 0.848 μm, at the ARM site $\rho_{0.858} = 0.289$, averaged over (25 km)^2 $\langle \rho_{0.858} \rangle = 0.292$ with std dev = 0.043.

linois, more than 50% of the year NDVI < 0.4, while for the ARM site in Oklahoma it is only a few months. Obviously, snow will destroy the retrieval method completely.

7. Validation

In addition to validation with retrievals from other ground-based measurements (MWR and MFRSR) that are illustrated in Figs. 7 and 8, we show a model-based validation where the true value of optical depth is known. We used 10 realizations of a 10-cascade fractal cloud model of broken clouds from Cahalan (1994) and Marshak et al. (1998); (see Fig. 2 captions for details).

The cloud fraction was 81% and the total number of nonzero cloud optical thicknesses was $0.81 \times 2^{10} \times 10 \approx 8300$. The average in-cloud τ was 13 with a standard deviation of 10.5. For simplicity, we had "black" and "bright" surface with albedos $\rho_{RED} = 0.0$ and $\rho_{NIR} = 0.5$, respectively. The domain averaged *retrieved* values for oblique illumination of SZA $= 60°$ and conservative scattering gave very close results of mean 13.1 (versus "true" value of 13) and standard deviation 10.8 (versus true value of 10.5).

Figure 12a shows a scatterplot of retrieved versus true optical depth on a pixel-by-pixel basis for a pixel size of 25 m. We see that while the NDCI method overestimates cloud optical depth values especially for $\tau > 20$
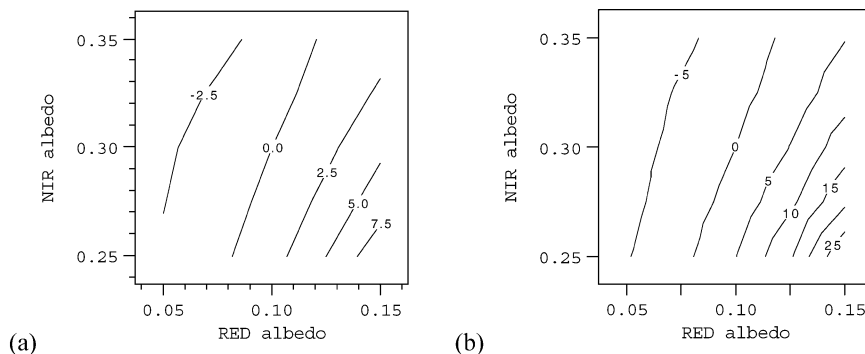

FIG. 10. Contour plots of the errors in the retrieved cloud optical depth due to incorrect surface albedos. Cimel measurements of 3 Jul 2002 (see Fig. 7a) are used. The reference surface albedo ($\rho_{RED} = 0.1$ and $\rho_{NIR} = 0.3$) is in the center of the both plots. It corresponds to the retrieved cloud optical depth τ^*. Let τ be the cloud optical depth inferred using "incorrect" albedos shown on horizontal and vertical axes. (a) The difference ($\tau - \tau^*$) averaged over all Cimel measurements of 3 Jul 2002; (b) the average relative difference, $100 \, (\tau - \tau^*)/\tau^* (\%)$.
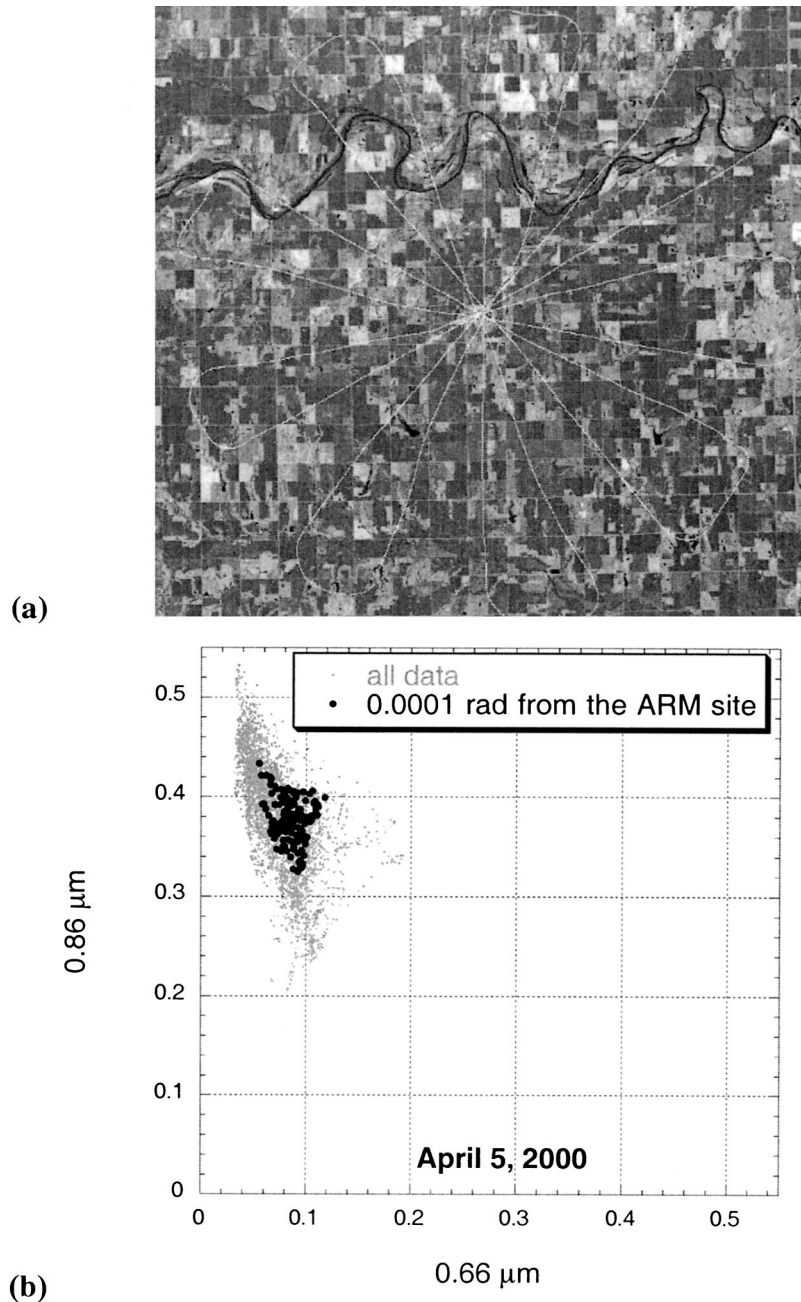
(a)

(b)

FIG. 11. Surface around the ARM site in Oklahoma. (a) Area around the ARM site with a daisy pattern flown by the Twin Otter aircraft on 5 Apr 2000 (courtesy of A. Trishchenko). (b) Surface albedo at 0.86 vs 0.66 μm measured from the aircraft by SSFR on 5 Apr 2000 [for details see Michalsky et al. (2003)]. Small gray dots correspond to all data collected around the area shown in (a) (roughly 10–15 km from the ARM site). Big black dots are the closest to the ARM site measurements (several middle points) taken within 0.0001 rad from the site (around 600 m). For them, $\langle \rho_{0.66} \rangle = 0.085$, std dev = 0.013, and $\langle \rho_{0.86} \rangle = 0.375$, std dev = 0.021.

and shows a lot of saturated values of $\tau = 100$, the RED versus NIR method gives on average unbiased estimates. Averaging over eight pixels (200-m-resolution pixels) substantially improves retrievals (Fig. 12b); the average

absolute pixel-by-pixel error in τ is 1.8 down from 2.4 (3.0 for in-cloud pixels) for 25-m-resolution pixels.

Finally, Figs. 13a and 13b illustrate histograms of cloud optical depth (true and retrieved) on a linear–
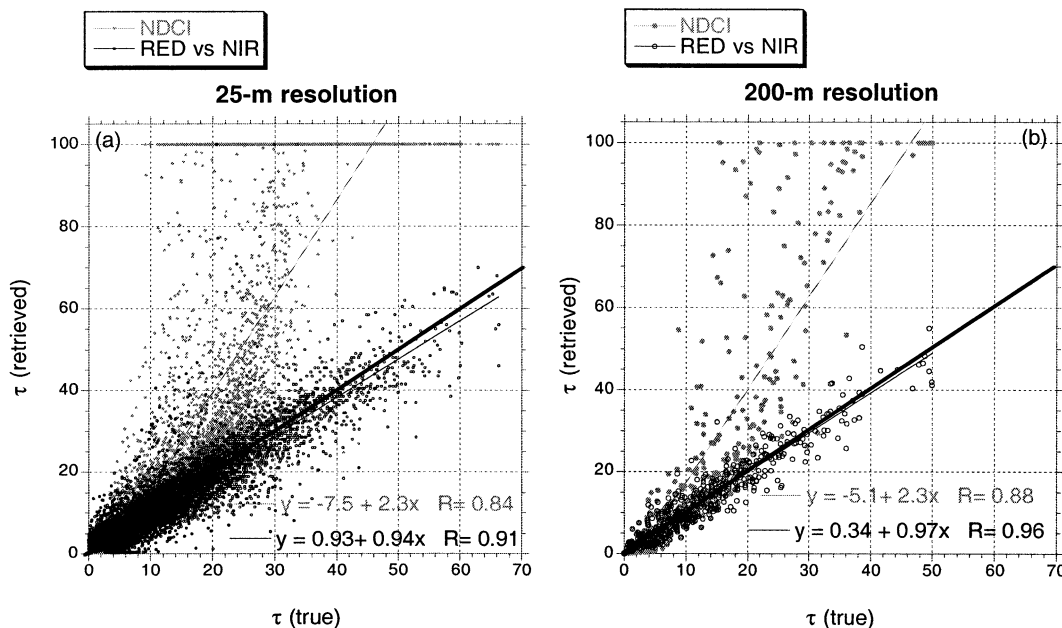
FIG. 12. Scatterplot of retrieved vs true cloud optical depth for the same bounded cascade model as in Fig. 2 (Cahalan 1994; Marshak et al. 1998). Total cloud fraction is 81%. Ten realizations of bounded cascades are used. SZA = 60°. Two retrieval methods are compared: the NDCI and the RED vs NIR. (a) Original resolution of 25 m. (b) Averaged over 200 m.

linear and log-linear scale, respectively. We can clearly see that the RED versus NIR method correctly retrieves the distribution of τ for both small and large values. Analyzing the cumulative histogram of absolute errors (Fig. 14), we can conclude that in 50% of the cases, the absolute error in the retrieval of optical depth is smaller than 1, in 75% of the cases smaller than 3, and in 90% of the cases, it is smaller than 5. In contrast, the NDCI method strongly overestimates the retrieved values for

at least $\tau > 40$; this makes it completely unacceptable for the retrieval of large τ.

8. Summary

Ground-based remote sensing of cloud optical properties with broadband pyranometers (e.g., Leontieva and Stamnes 1994) and/or narrowband radiometers (Min and Harrison 1996) that measure downwelling fluxes is lim-
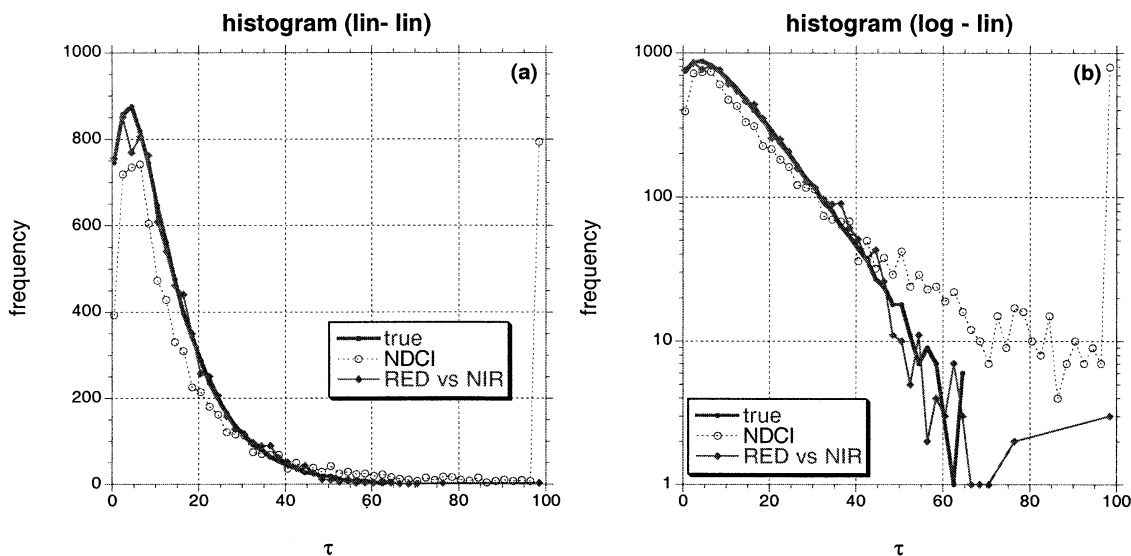

FIG. 13. Histogram of cloud optical depth τ from Fig. 12a. Pixel resolution is 25 m: (a) linear–linear plot; (b) log–linear plot.
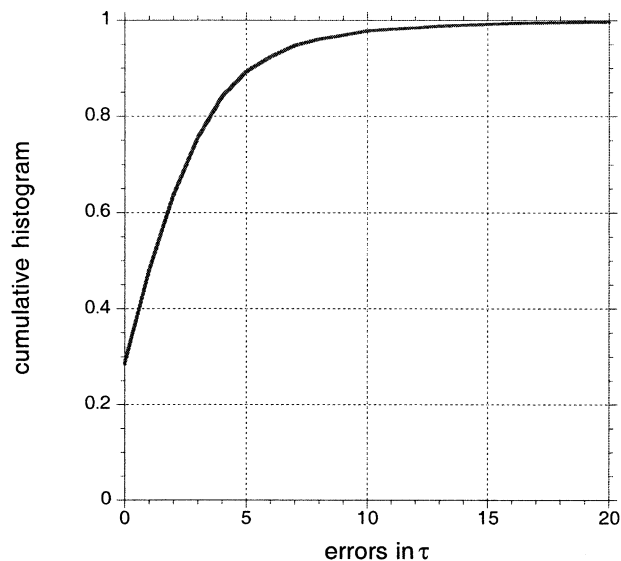
FIG. 14. Cumulative histogram of absolute errors in the retrieval of cloud optical depth from Fig. 12a. Pixel resolution is 25 m.

ited to overcast conditions (Boers et al. 2000). Retrieved values of cloud optical depth have an effective rather than a local character (Barker and Marshak 2001). Monochromatic narrow-field-of-view measurements are not widely applicable for retrieval because cloud optical depth is a two-valued function of zenith radiance. Among others these shortcomings prevent us from creating a ground-based cloud properties monitoring network, such as the AERONET, for assessing aerosol properties (Holben et al. 1998).

To remove the ambiguity in measured downwelling radiance, it was suggested to exploit a spectral contrast in surface properties between RED and NIR spectral regions (Marshak et al. 2000). The algebraic combination of NIR and RED zenith measurements such as normalized difference cloud index (NDCI) largely removes not only the double-valued relationship between radiance and optical depth but also the radiative effects of the 3D cloud structure. However, for accurate retrievals it requires additional information on downwelling fluxes (Barker and Marshak 2001; Barker et al. 2002) and the NDCI (or other similar indices) alone cannot be used for broken cloud conditions and thick clouds.

Here we proposed a new method that overcomes the limitations of the NDCI; instead of using one value of an algebraic combination between two wavelengths, we use both wavelengths independently in the NIR versus RED plane. Mapping NIR and RED measurements of zenith radiance into a two-dimensional plane-parallel radiative-transfer-based lookup table (LUT) allowed us not only to retrieve cloud optical depth τ but also to estimate cloud fraction A_c. However, since plane-parallel radiative transfer is unable to fit all 3D measurements (e.g., leakage from cloud edges results in cloud transmittance larger than unity), instead of a real cloud fraction (the ratio of cloudy pixels to the total number of pixels), we retrieve a radiatively *effective* cloud fraction that also accounts for cloud internal structure and matches 3D measurements with 1D calculations. This does not preclude it from being *negative*. The retrieved values A_c are not used per se but serve as a degree of cloud inhomogeneity for the retrieval of cloud optical depth.

This method assumes that surface albedo in both RED and NIR spectral regions is known. Because of the proposed *global* character of the cloud monitoring network, the high-and moderate-resolution satellite data are the only available source of surface properties. As an example, here we use MODIS and MISR data to obtained surface albedo for the ARM site. Even in case of heterogeneous surface as the one around the ARM site in Oklahoma (Li et al. 2002; Michalsky et al. 2003), we found that the proposed method can be successfully used since the local surface properties are less important than their average characteristics (Knyazikhin and Marshak 2000). This suggests that an operational algorithm for retrieval cloud optical depth from AERONET can use MODIS and/or MISR products to routinely update surface albedo.

In addition to the comparison with MFRSR (courtesy of Q. Min 2003, personal communication) and MWR retrievals (the latter needs an assumption on the drop size) that are located next to the Cimel at the ARM site, we used realizations of a fractal model of cloud inhomogeneity (Cahalan 1994; Marshak et al. 1994) and of broken clouds (Marshak et al. 1998). Since the true optical depth was known, we were able to asses the performance of the proposed method. We found that 75% of the retrieved optical depth out of about 10 000 pixels with 25-m resolution had absolute errors smaller than 3. Averaging over 200 m substantially improves the retrieval.

To conclude, the preliminary results look very promising both theoretically and from measurements. As soon as the method matures, it will be systematically applied to AERONET "cloud" measurements that are inappropriate for aerosol studies to monitor cloud optical depth.

REFERENCES

Barker, H. W., and A. Marshak, 2001: Inferring optical depth of broken clouds above green vegetation using surface solar radiometric measurements. *J. Atmos. Sci.,* **58,** 2989–3006.

——, ——, W. Szyrmer, A. Trishchenko, J.-P. Blanchet, and Z. Li, 2002: Inference of cloud optical properties from aircraft-based solar radiometric measurements. *J. Atmos. Sci.,* **59,** 2093–2111.

Boers, R., 1997: Simultaneous retrievals of cloud optical depth and droplet concentration from solar irradiance and microwave liquid. *J. Geophys. Res.,* **102,** 29 881–29 891.

——, A. van Lammeren, and A. Feijt, 2000: Accuracy of optical depth retrieval from ground-based pyranometers. *J. Atmos. Oceanic Technol.,* **17,** 916–927.

Bothwell, G. W., E. G. Hansen, R. E. Vargo, and K. C. Miller, 2002: The Multi-angle Imaging SpectroRadiometer science data system, its products, tools, and performance. *IEEE Trans. Geosci. Remote Sens.,* **40,** 1467–1476.

Box, M. A., S. A. W. Gerstl, and C. Simmer, 1988: Application of the adjoint formulation to the calculation of atmospheric radiative effects. *Beitr. Phys. Atmos.,* **61,** 303–311.

Cahalan, R. F., 1994: Bounded cascade clouds: Albedo and effective thickness. *Nonlinear Proc. Geophys.,* **1,** 156–167.

Diner, D. J., and Coauthors, 1999: New directions in earth observing: Scientific applications of multiangle remote sensing. *Bull. Amer. Meteor. Soc.,* **80,** 2209–2228.

Dong, X., T. P. Ackerman, E. E. Clothiaux, P. Pilewskie, and Y. Han, 1997: Microphysical and radiative properties of boundary layer stratiform clouds deduced from ground-based measurements. *J. Geophys. Res.,* **102,** 23 829–23 843.

Holben, B. N., and Coauthors, 1998: AERONET—A federated instrument network and data archive for aerosol characterization. *Remote Sens. Environ.,* **66,** 1–16.

Kaufmann, R. K., L. Zhou, Y. Knyazikhin, N. Shabanov, R. B. Myneni, and C. J. Tucker, 2000: Effect of orbital drift and sensor changes on the time series of AVHRR vegetation index data. *IEEE Trans. Geosci. Remote Sens.,* **38,** 2584–2597.

Knyazikhin, Y., and A. Marshak, 2000: Mathematical aspects of BRDF modeling: Adjoint problem and Green's function. *Remote Sens. Rev.,* **18,** 263–280.

——, J. V. Martonchik, D. J. Diner, R. B. Myneni, M. M. Verstraete, B. Pinty, and N. Gobron, 1998: Estimation of vegetation canopy leaf area index and fraction of absorbed photosynthetically active radiation from atmosphere-corrected MISR data. *J. Geophys. Res.,* **103,** 32 239–32 256.

Leontieva, E., and K. Stamnes, 1994: Estimations of cloud optical thickness from ground-based measurements of incoming solar radiation in the Arctic. *J. Climate,* **7,** 566–578.

——, and ——, 1996: Remote sensing of cloud optical properties from ground-based measurements of transmittance: A feasibility case. *J. Appl. Meteor.,* **35,** 2012–2022.

Li, Z.-Q., M. C. Cribb, and A. P. Trishchenko, 2002: Impact of surface inhomogeneity on solar radiative transfer under overcast conditions. *J. Geophys. Res.,* **107,** 4294, doi:10.1029/2001JD000976.

Marshak, A., A. Davis, R. F. Cahalan, and W. J. Wiscombe, 1994: Bounded cascade models as non-stationary multifractals. *Phys. Rev.,* **49E,** 55–69.

——, ——, W. J. Wiscombe, W. Ridgway, and R. F. Cahalan, 1998: Biases in shortwave column absorption in the presence of fractal clouds. *J. Climate,* **11,** 431–446.

——, L. Oreopoulos, A. Davis, W. Wiscombe, and R. Cahalan, 1999: Horizontal radiative fluxes in clouds and accuracy of the Independent Pixel Approximation at absorbing wavelengths. *Geophys. Res. Lett.,* **26,** 1585–1588.

——, Y. Knyazikhin, A. Davis, W. Wiscombe, and P. Pilewskie, 2000: Cloud–vegetation interaction: Use of normalized difference cloud index for estimation of cloud optical thickness. *Geophys. Res. Lett.,* **27,** 1695–1698.

Michalsky, J., Q. Min, J. Barnard, R. Marchand, and P. Pilewskie, 2003: Simultaneous spectral albedo measurements near the Atmospheric Radiation Measurement Southern Great Plains (ARM SGP) central facility. *J. Geophys. Res.,* **108,** 4254, doi:10.1029/2002JD002906.

Min, Q. L., and L. C. Harrison, 1996: Cloud properties derived from surface MFRSR measurements and comparison with GOES results at the ARM SGP site. *Geophys. Res. Lett.,* **23,** 1641–1644.

Nakajima, T. Y., and M. D. King, 1990: Determination of the optical thickness and effective particle radius of clouds from reflected solar radiation measurements. Part I: Theory. *J. Atmos. Sci.,* **47,** 1878–1893.

Pavloski, C. F., and T. P. Ackerman, 1999: High speed cloud optical depth retrievals from a narrow field of view, narrowband, shortwave zenith pointing radiometer. *Proc. Ninth Atmospheric Radiation Measurement* (ARM) *Science Team Meeting,* San Antonio, TX, U.S. Dept. of Energy. [Available online at http://www.arm.gov/docs/documents/technical/conf_9903/pavloski-99.pdf.]

——, E. E. Clothiaux, H. W. Barker, A. Marshak, and T. P. Ackerman, 2002: Field test of the cloud-surface interaction based broken cloud field optical depth retrieval: Results from the ARM SGP 2001 Summer–Fall NFOV campaign. *Proc. 12th ARM Science Team Meeting,* St. Petersburg, FL, U.S. Dept. of Energy.

Pilewskie, P., A. F. H. Goetz, D. A. Beal, R. W. Bergstrom, and P. Mariani, 1998: Observations of the spectral distribution of solar irradiance at the ground during SUCCESS. *Geophys. Res. Lett.,* **25,** 1141–1144.

Ricchiazzi, P., C. Gautier, and D. Lubin, 1995: Cloud scattering optical depth and local surface albedo in the Antarctic—Simultaneous retrieval using ground-based radiometry. *J. Geophys. Res.,* **100,** 21 091–21 104.

Schaaf, C. B., and Coauthors, 2002: First operational BRDF, albedo nadir reflectance products from MODIS. *Remote Sens. Environ.,* **83,** 135–148.

Shabanov, N. V., L. Zhou, Y. Knyazikhin, C. J. Tucker, and R. B. Myneni, 2002: Analysis of interannual changes in northern vegetation activity observed in AVHRR data during 1981 to 1994. *IEEE Trans. Geosci. Remote Sens.,* **40,** 115–130.

Stamnes, K., S.-C. Tsay, W. J. Wiscombe, and K. Jayaweera, 1988: Numerically stable algorithm for discrete-ordinate-method radiative transfer in multiple scattering and emitting layered media. *Appl. Opt.,* **27,** 2502–2512.

Tian, Y., Y. Zhang, Y. Knyazikhin, R. B. Myneni, J. Glassy, G. Dedieu, and S. W. Running, 2000: Prototyping of MODIS LAI and FPAR algorithm with LASUR and LANDSAT data. *IEEE Trans. Geosci. Remote Sens.,* **38,** 2387–2401.

Titov, G. A., 1998: Radiative horizontal transport and absorption in stratocumulus clouds. *J. Atmos. Sci.,* **55,** 2549–2560.

Tucker, C. J., 1979: Red and photographic infrared linear combination for monitoring vegetation. *Remote Sens. Environ.,* **8,** 127–150.

Verstraete, M. M., and B. Pinty, 1996: Designing optical spectral indexes for remote sensing applications. *IEEE Trans. Geosci. Remote Sens.,* **34,** 1254–1265.

Wiscombe, W., A. Marshak, Y. Knyazikhin, and A. Davis, 2000: The use of reflection from vegetation for estimating broken-cloud optical depth. *Proc. 10th Atmospheric Radiation Measurement (ARM) Science Team Meeting,* San Antonio, TX, U.S. Dept. of Energy. [Available online at http://www.arm.gov/docs/documents/technical/conf_0003/wiscombe-wj.pdf.]